

Plasmon-induced thermal tuning of few-exciton strong coupling in 2D atomic crystals

LIN LIU,^{1,†} LANDOBASA Y. M. TOBING,^{1,†}  TINGTING WU,¹ BO QIANG,¹ FRANCISCO J. GARCIA-VIDAL,^{2,3}  DAO HUA ZHANG,^{1,5} QI JIE WANG,^{1,6} AND YU LUO^{1,*} 

¹School of Electrical & Electronic Engineering, Nanyang Technological University, Singapore 639798, Singapore

²Departamento de Física Teórica de la Materia Condensada and Condensed Matter Physics Center (IFIMAC), Universidad Autónoma de Madrid, 28049 Madrid, Spain

³Institute of High Performance Computing, Agency for Science, Technology, and Research (A*STAR), Singapore 138632, Singapore

⁵e-mail: edhzhang@ntu.edu.sg

⁶e-mail: qjwang@ntu.edu.sg

*Corresponding author: luoyu@ntu.edu.sg

Received 12 July 2021; revised 31 August 2021; accepted 23 September 2021 (Doc. ID 436140); published 3 November 2021

Strong light–matter interaction in 2D materials at the few-exciton level is important for both fundamental studies and quantum optical applications. Characterized by a fast coherent energy exchange between photons and excitons, strongly coupled plasmon–exciton systems in 2D materials have been reported with large Rabi splitting. However, large Rabi splitting at the few-exciton level generally requires large optical fields in a highly confined mode volume, which are difficult to achieve for in-plane excitons in 2D materials. In this work, we present a study of a strongly coupled gold dimer antenna with a sub-10 nm gap on a monolayer tungsten disulphide (WS₂), with an estimated number of excitons of 4.67 ± 0.99 . We demonstrate that varying the spatial mode overlap between the plasmonic field and the 2D material can result in up to a \sim tenfold increase in the number of excitons, a value that can be further actively tuned via plasmon-induced heating effects. The demonstrated results would represent a key step toward quantum optical applications operating at room temperatures. © 2021 Optical Society of America under the terms of the [OSA Open Access Publishing Agreement](#)

<https://doi.org/10.1364/OPTICA.436140>

1. INTRODUCTION

Interaction of highly confined electromagnetic fields with quantum emitters has spurred much interests in both fundamental studies [1–7] and applications [8–12]. Due to their strong spatiotemporal field confinement, plasmonic nanocavities are excellent candidates for light–matter interaction, notably because of their large photonic density of states ($\text{LDOS} \propto Q/V_{\text{mod}}$), characterized by the resonance Q-factor and the mode volume V_{mod} . Plasmon–exciton systems are widely employed to investigate strong coupling in different excitonic platforms, such as with dye molecules [13–15], quantum dots [16,17], J-aggregates [18–22], and 2D materials [23,24]. In strongly coupled systems, the coherent energy exchange between photons and excitons manifests in the so-called Rabi splitting [25–28] in the spectrum, which is also used to gauge their interaction strength.

Strongly coupled plasmon–exciton systems in 2D materials and colloidal quantum dots with Rabi splitting as large as $\sim 200 - 400$ meV have been demonstrated [29–32]. However, the cause for such large splitting is not clearly attributed to the large photonic density of states because the plasmon–exciton coupling occurs not just for single exciton but many excitons enclosed by the spatial extent of the cavity mode. This is because the coupling strength g_N of a uniform cavity mode and N identical excitons

scales as $g_N = \sqrt{N}(\vec{\mu}_e \cdot \vec{E}_{\text{cav}})$, with $\vec{\mu}_e$ being the transition dipole moment of the emitter, \vec{E}_{cav} the cavity vacuum E -field, and N the number of excitons. Most of the plasmon–exciton systems with large Rabi splitting are associated with a large number of excitons, notably for nanoparticle-on-mirror (NPoM) coupled with 2D materials [33–35]. As the resonance modes of NPoM structures are characteristically dominated by out-of-plane E -fields [33,36], the coupling with the in-plane transition dipole of the 2D material is likely to be small. However, the mode area of the NPoM cavity mode is typically much larger than those of the planar nanoantenna, thus effectively increasing the number of excitons involved in the coupling, and consequently the Rabi splitting.

Reducing the number of excitons in the strong-coupling regime is crucial from the quantum optical perspective where the interaction between a single photon and a single exciton is highly desired. Efforts have been devoted to achieve strong coupling down to the single exciton level. Liu *et al.* investigated the strong coupling of chemically synthesized Au–Ag nanorods with monolayer coating of J-aggregate in water suspension [37]. Santhosh *et al.* reported strong coupling with a single quantum dot in a planar silver bowtie nanoantenna, via deterministic placements of colloidal quantum dots [38]. Chikkaraddy *et al.* demonstrated strong coupling approaching the single molecule level in an NPoM system coupled

with dye molecules, whose transition dipole moments are in the out-of-plane [39]. Meanwhile, strong coupling with 2D materials have been demonstrated in NPoM systems, yet with hundreds of excitons involved [34,40]. This is expected from the dominant out-of-plane mode fields that are not coupled effectively with the in-plane excitons of the 2D materials. Due to their direct bandgaps and strong exciton binding energies, light–matter interaction in monolayer transition metal dichalcogenides (TMD) also has been widely investigated, notably as polaritonic platforms at room temperature [23,24]. Realizing large Rabi splitting at the few-exciton level ($N < 10$) in 2D materials would represent an important advance toward quantum optical applications operating at room temperature, yet remains challenging because it requires a large in-plane electric field in a highly confined mode volume to boost the coupling strength.

In this work, we present a detailed investigation of a strongly coupled plasmon–exciton system consisting of isolated planar dimer antennas and 2D WS₂ at the few-exciton level. By decreasing the dimer gap spacing to the sub-10 nm range, the number of excitons involved in the coupling is reduced. Importantly, the in-plane cavity mode field of our planar gold dimers is much larger than that of the NPoM architectures. We find a significant dependence of the number of TMD excitons in the system (N), and therefore the Rabi splitting, on temperature via plasmon-induced heating and other thermal effects in the hybrid TMD-antenna system. We observe an increase from $N = 4.67 \pm 0.99$ to $N = 7.69 \pm 1.07$ as the incident intensity is varied from 215 mW/cm² to 456 mW/cm². In addition, we observed a tenfold increase in the number of excitons involved in the strong coupling as the interaction strength is decreased by inserting an ultrathin spacer layer between the dimer and the TMD, thereby illustrating the confounding effects of the plasmonic mode field and number of excitons in the observed Rabi splitting. We further investigate the intensity-dependent thermal effects in the red shifting of the anti-crossing characteristics and photoluminescence (PL) intensity enhancement at an increasing pump intensity, while also discussing its feasibility as an active tuning mechanism.

2. RESULTS AND DISCUSSION

Figure 1(a) depicts the schematics of the plasmon–exciton system, which consists of a planar dimer nanoantenna lithographically fabricated on a monolayer tungsten disulfide (WS₂) grown by chemical vapor deposition (CVD) on a SiO₂/Si substrate. Sparse arrays of plasmonic dimers were realized at 4 μm periodicities by electron beam lithography (EBL), followed by the sonicated cold development approach (see Appendix A.1, Sample Fabrication). The 4 μm inter-antenna spacing was chosen to ensure negligible couplings among the dimers, because it is much larger than the scattering cross-sections of a plasmon dimer, which is typically in the few hundred nm² range. This choice of 4 μm periodicity also enables us to characterize the photoluminescence properties of each element independently under a laser illumination with a ~1 μm spot size. For all antenna considered in this work, the dimer thickness (t) is set to 30 nm, while the dimer size (s) is varied from 60 nm to 100 nm. The dimer gap spacing (d) is tuned from ~20 nm to the sub-10 nm range by carefully adjusting the exposure dose.

The dark-field scattering images of the dimers coupled to TMD, obtained through hyperspectral imaging measurements

(see Appendix A.2, Optical Characterization), are presented in Fig. 1(b), where the red spots correspond to individual antennas. The bright-field image of an uncoupled dimer on SiO₂/Si (brown) and coupled dimer on WS₂ monolayer (light purple) is presented in Fig. 1(c). The dark purple dots correspond to the sparse distribution of gold antennas. The dark-field scattering spectra of dimers coupled (red) and uncoupled (blue) to WS₂ excitons are shown in Fig. 1(d), exhibiting a clear symmetrical splitting for the coupled case, characterized by split resonances (E_{\pm}), their respective linewidth (γ_{\pm}), and Rabi splitting (Ω). Phenomenologically, the plasmon–exciton coupling can be understood from the Jaynes–Cummings Hamiltonian [41,42], which yields the eigenvalue problem for the hybrid states (α , β)

$$\begin{pmatrix} \omega_{\text{pl}} + \frac{i\gamma_{\text{pl}}}{2} & g \\ g & \omega_{\text{ex}} + \frac{i\gamma_{\text{ex}}}{2} \end{pmatrix} \begin{pmatrix} \alpha \\ \beta \end{pmatrix} = \omega_{\pm} \begin{pmatrix} \alpha \\ \beta \end{pmatrix}, \quad (1)$$

with ω_{pl} and ω_{ex} as the plasmonic mode and exciton frequencies, γ_{pl} and γ_{ex} as the damping loss of the plasmonic resonance and exciton emission linewidth, and g as the measured coupling strength between the plasmon mode and excitons. The linewidth of the CVD-grown WS₂ is found to be $\gamma_{\text{ex}} = 67$ meV, while the range of the Q -factor of the dimer mode ($Q = \omega_{\text{pl}}/\gamma_{\text{pl}}$) is ~8–9. Based on this, the observed eigenfrequencies for the hybrid, polaritonic, modes can be expressed as

$$\omega_{\pm} = \frac{1}{2} (\omega_{\text{pl}} + \omega_{\text{ex}}) \pm \sqrt{g^2 + \frac{\delta^2}{4}}, \quad (2)$$

with $\delta = \omega_{\text{pl}} - \omega_{\text{ex}}$ as the experimental detuning between the plasmon mode and the exciton energy. The split resonances (ω_{\pm}) versus resonance detuning (δ) for Au dimers with different dimensions were compiled and then presented as anti-crossing curves in Fig. 2(a). Since the optical response of the dimer changes due to its coupling with the WS₂, the experimental detuning was extracted from the split resonances by $\delta_{\text{exp}} = \omega_{+} + \omega_{-} - 2\omega_{\text{ex}}$. The exciton frequency is fixed at $\omega_{\text{ex}} = 2.02$ eV, as verified by photoluminescence and differential reflectance measurements (Fig. S3 in Supplement 1). To investigate the plasmon–exciton coupling in more detail, we also characterize the anti-crossing properties in different spatial mode overlap situations, achieved by incorporating a 2 nm dielectric spacer between the dimer and WS₂ [Fig. 2(b)]. For simplicity, we denote these two spatial overlap situations as the TMD dimer (for the bare WS₂) and TMD spacer dimer (for the 2 nm spacer). The plasmonic resonance frequency is tuned by both the dimer size and gap spacing, which can be varied through the e -beam exposure dose in the fabrication process. The latter is varied by increasing the longitudinal dipolar coupling (by decreasing the gap spacing). Increasing the size and decreasing the gap spacing can be carried out simultaneously by increasing the EBL exposure dose. This is illustrated in Fig. 2(c) (for the TMD dimer), which shows a progressive red shift as the gap spacing decreases from ~18 nm to the sub-10 nm range, and the size increases from ~111 nm to ~123 nm, associated with an increase of the exposure dose from 292 pC/cm to 328 pC/cm (for a dimer with nominal dimensions of $s = 100$ nm and $d = 20$ nm).

Anti-crossing curves under two different incident intensities are investigated, with the Rabi splitting obtained from fitting the anti-crossing curves with Eq. (2). Under 215 mW/cm² illumination (circle markers), the Rabi splittings are found to be $\Omega_0 = 115.2 \pm 12.2$ meV (for the TMD dimer) and $\Omega_d =$

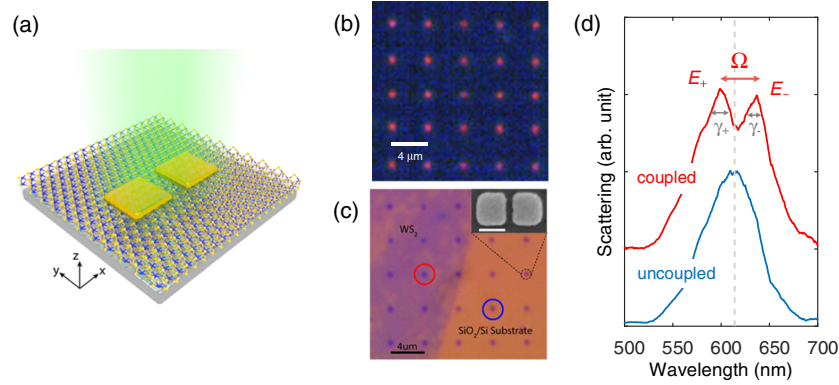


Fig. 1. Plasmon–exciton systems of gold dimer nanoantenna on monolayer transition metal dichalcogenide. (a) Schematic of gold dimer on CVD-grown tungsten disulphide (WS_2) on SiO_2/Si substrate. (b) Dark-field and image of isolated TMD-dimer systems at sparse periodicity of $4 \mu\text{m}$. (c) Bright-field image of coupled and uncoupled dimers, with their scattering spectra shown in (d), where 2 nm thick Al_2O_3 layer is inserted between the dimer ($s = 80 \text{ nm}$, $d = 40 \text{ nm}$) and the WS_2 . The observable linewidths and Rabi splitting were found as $\gamma_+ = 66.4 \text{ meV}$, $\gamma_- = 46.4 \text{ meV}$, $g = 58.02 \text{ meV}$, and $\Omega = 116.05 \text{ meV}$. The inset shows the exemplary SEM images of the fabricated dimer with nominal dimensions of $s = 100 \text{ nm}$ and $d = 16 \text{ nm}$. The scale bar in the inset represents 100 nm .

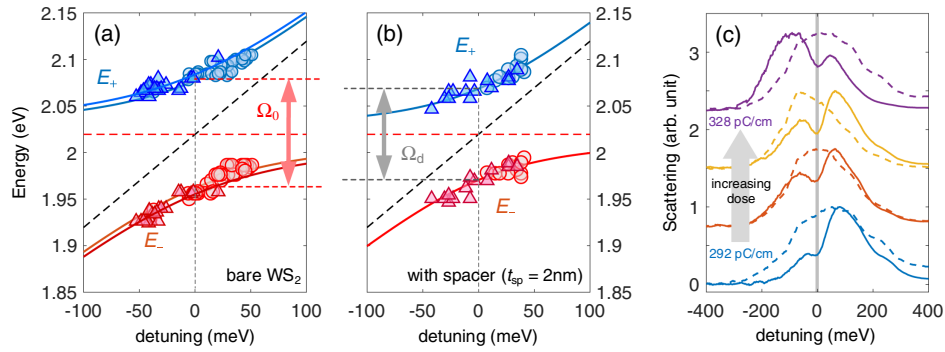


Fig. 2. Anti-crossing characteristics of individual dimers at different incident Hg lamp intensities: (a) TMD dimer, $\Omega_0(I = 215 \text{ mW}/\text{cm}^2) = 115.2 \pm 12.2 \text{ meV}$ (circles), $\Omega_0(I = 456 \text{ mW}/\text{cm}^2) = 128.6 \pm 9 \text{ meV}$ (triangles); (b) TMD spacer dimer (with 2 nm spacer), $\Omega_d(I = 215 \text{ mW}/\text{cm}^2) = 100.2 \pm 12 \text{ meV}$ (circles), $\Omega_d(I = 456 \text{ mW}/\text{cm}^2) = 100.7 \pm 12.4 \text{ meV}$ (triangles). The y axes of (a–b) is the energy (eV). (c) The dark-field scattering spectra of TMD-dimer (solid) and uncoupled dimer (dashed) with nominal $s = 100 \text{ nm}$ and $d = 20 \text{ nm}$ at decreasing gap from $d = 18 \pm 3 \text{ nm}$ toward $d = 9 \pm 3 \text{ nm}$ (sub- 10 nm), and increasing size from $s = 111 \pm 4 \text{ nm}$ toward $s = 123 \pm 4 \text{ nm}$; achieved by increasing the exposure dose from $292 \text{ pC}/\text{cm}$ to $328 \text{ pC}/\text{cm}$.

$100.2 \pm 12 \text{ meV}$ (for the TMD spacer dimer). As the illumination intensity is increased to $456 \text{ mW}/\text{cm}^2$ (triangle markers), we found that the Rabi splitting changes to $\Omega_0 = 128.6 \pm 9 \text{ meV}$ (for the TMD dimer) and $\Omega_d = 100.7 \pm 12.4 \text{ meV}$ (for the TMD spacer dimer). Given that the coupling strength is independent from the incident intensity, the larger Rabi splitting at a higher intensity is indicative of the thermal effects caused by the plasmonic resonance. It is also interesting to note that the increase in Rabi splitting is statistically significant only for the TMD dimer system, suggesting the dependence of such thermal effects on plasmonic field enhancement in the TMD plane. Such thermal effects can also be seen in the spectral movements from circle to triangle markers in Figs. 2(a) and 2(b).

The strong coupling criteria [30], $\Omega > (\gamma_+ + \gamma_-)/2$, with γ_{\pm} as the linewidths of the split polaritonic modes, are investigated for all the TMD dimer and TMD spacer dimer systems in this study. Figure 3 presents the mapping of the Rabi splitting as a function of the upper polariton band (UPB, E_+) and lower polariton band (LPB, E_-). The TMD dimer and TMD spacer dimer cases are denoted by the red and green markers, respectively. The strong coupling criteria are represented by the white bands (for the TMD dimer) and green bands (for the TMD spacer dimer), with the

bands denoting the standard deviations in our experimental measurements. The zero-detuning line $\delta = 0$, at which the resonance splitting is the most symmetrical, is depicted by the red dashed line. The positions of (E_+ , E_-), which are far from the strong coupling criteria bands, indicating that all the TMD dimer and TMD spacer dimer systems in our work are in the strong coupling regime. The (E_+ , E_-) corresponding to $215 \text{ mW}/\text{cm}^2$ (circles) and $456 \text{ mW}/\text{cm}^2$ (triangles) lamp intensities are also presented, indicating the movements of (E_+ , E_-) data across the zero-detuning line, similar to those in Figs. 2(a) and 2(b). The increase in the incident intensity imparts red shifting to the resonance modes, due to the plasmon-induced thermal effects. It is interesting to note that, unlike the TMD-dimer case, the (E_+ , E_-) positions for TMD-spacer-dimer case are mostly above the detuning line. This is likely due to the refractive index difference between Al_2O_3 (~ 1.767) and monolayer WS_2 (~ 4.294) around $\sim 2 \text{ eV}$, yielding a blue shift to the resonance modes of the dimers with a 2 nm thick spacer.

The number of excitons involved in the coupling is estimated as follows. For N excitons coupled to plasmon mode, the coupling strength is $g_N = \sqrt{N}\mu_e|E_{\text{cav}}|$, where μ_e is the transition

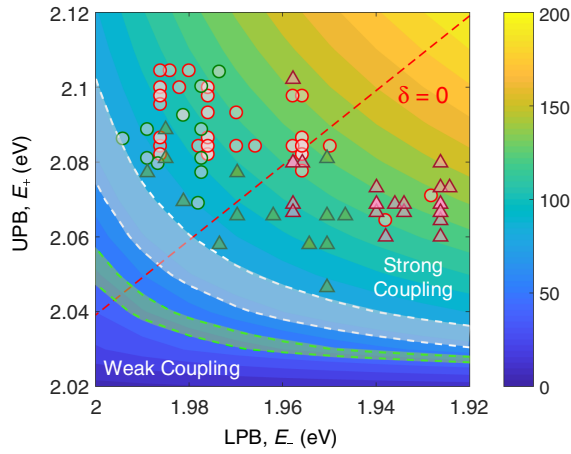


Fig. 3. Mapping of Rabi splitting for plasmon–exciton systems with different field overlaps and lamp intensities. Dimers coupled to bare WS₂ (red markers) and WS₂ with 2 nm thick dielectric spacer (green markers) were investigated at 215 mW/cm² (circles) and 456 mW/cm² (triangles). The boundaries between weak and strong coupling are denoted by the white band (for bare WS₂) and green band (for WS₂ with dielectric spacer). The zero detuning, at which the spectrum is the most symmetrical is indicated by the zero-detuning line $\delta = 0$ (red dashed line).

dipole moment of the exciton, and $|E_{\text{cav}}|$ is the E -field of the cavity mode normalized to vacuum energy. Using the energy density $W(r) = \frac{1}{2} \text{Re} \left(\frac{d[\omega\epsilon]}{d\omega} \right) |E_{\text{cav}}|^2 + \frac{1}{2} \mu_0 |H_{\text{cav}}|^2$ to calculate the energy stored in a cavity, and equate it with the photon energy in quantum optics formalism, one has $\int W(r) d^3r = \hbar\omega(n + 1/2)$. Using $\int W(r) d^3r \equiv \epsilon_0 \epsilon |E_{\text{cav}}|^2 V_{\text{mod}}$, with $V_{\text{mod}} = \int d^3r W(r) / \max[W(r)]$ as the mode volume, one can arrive at the familiar expression for the vacuum cavity field ($n = 0$) $|E_{\text{cav}}| = \sqrt{\hbar\omega / (2\epsilon_0 \epsilon V_{\text{mod}})}$ [43], at exciton energy ($\omega = \omega_{\text{exc}}$). However, this may not be accurate for 2D materials as the light–matter interaction occurs only at the TMD plane, and due to the fact that plasmonic fields are highly concentrated at plasmonic hot spots. In addition, excitons in 2D materials are spatially delocalized [36], instead of being “point-like” dipoles as in the case of colloidal quantum dots. The coherence diameter of 2D exciton is given by $d_c = 8\hbar\sqrt{\pi} / (M\Delta)$ [44], where $M = m_e^* + m_h^*$ is the total exciton mass and Δ is the exciton emission linewidth. For the CVD-grown monolayer WS₂ in this work, where $\Delta \sim 67$ meV and $M = 0.64m_0$ [45], the coherence diameter is found to be $d_c \sim 19$ nm. This is comparable to the sub-20 nm gap spacings and the size of the plasmonic hotspots of our lithographically fabricated dimer nanoantenna.

The plasmon–exciton coupling strength in a 2D TMD can thus be written as $g_N = \sqrt{N} \mu_e |E_{xy}|$, where the total cavity field (E_{cav}) is replaced with the in-plane cavity E -field (E_{xy}) since the plasmon–exciton interaction occurs only with the in-plane transition dipole moments of the TMD. Using the same vacuum energy normalization, we deduce the normalizing factor F for the simulated cavity field, $|E_{\text{cav}}| = F |E_{\text{tot}}|$, such that $F^2 \int W_{\text{sim}} d^3r = \hbar\omega/2$. Here, $|E_{\text{tot}}|$ is the simulated total E -field and $W_{\text{sim}}(r) = \frac{1}{2} \text{Re} \left(\frac{d[\omega\epsilon]}{d\omega} \right) |E_{\text{tot}}|^2 + \frac{1}{2} \mu_0 |H_{\text{tot}}|^2$ is the simulated energy density at $\omega = \omega_{\text{exc}}$. Based on this, the normalized cavity field is $E_{\text{cav}}(x, y) = |E_{\text{tot}}(x, y)| \sqrt{\hbar\omega / (2 \int W_{\text{sim}} d^3r)}$, and the position-dependent coupling strength is thus given by

$$g_0(x, y) = \mu_e \sqrt{E_{\text{tot}}^2(x, y) - E_z^2(x, y)} \sqrt{\frac{\hbar\omega}{2 \int W_{\text{sim}} d^3r}}, \quad (3)$$

with $|E_{xy}(x, y)| = \sqrt{E_{\text{tot}}^2(x, y) - E_z^2(x, y)}$ as the in-plane simulated E -fields in the TMD plane. The number of excitons is thus deduced by $N = (g_{\text{exp}}/g_{\text{avg}})^2$, which has the standard deviation of $\Delta N = 2g_{\text{exp}} \Delta g_{\text{exp}} / g_{\text{avg}}^2$. Here, $g_{\text{exp}} = \Omega_{\text{exp}}/2$ is the experimentally obtained coupling strength, and g_{avg} is the spatially averaged coupling strength in the TMD plane, given by

$$g_{\text{avg}} = \sqrt{\frac{\int_S g_0^2 dS}{A_{\text{mod}}}}, \quad (4)$$

where $A_{\text{mod}} = \int W d^2r / \max[W(r)]$ is the mode area calculated in the TMD plane. As the range of the mode area is $A_{\text{mod}} \sim 10^{-3}(\lambda/n)^2$ for our dimers, the plasmon–exciton coupling occurs mostly at plasmonic hotspots, leading to $g_{\text{avg}} \lesssim g_{\text{max}}$. For this, the number of excitons can alternatively be estimated by g_{max} .

The normalized scattering responses of the strongly coupled plasmon–exciton systems for different spatial field overlaps are shown in Fig. 4(a), with the mapping of coupling strengths $g_0(x, y)$ [g -field in Eq. (3)], presented in Figs. 4(b) and 2(c) for TMD dimer and TMD spacer dimer cases, respectively. The experimental value for the transition dipole moment of monolayer WS₂ was taken from Sie *et al.* [45]; i.e., $\mu_e = 56D$. The split resonances for the TMD dimer case are more prominent than that of the TMD spacer dimer, as expected from the weaker coupling of the latter. The number of excitons (N) for the TMD dimer is found to be $N = 4.67 \pm 0.99$ (at 215 mW/cm²) and $N = 7.69 \pm 1.07$ (at 456 mW/cm²). Meanwhile, for the TMD spacer dimer cases, we have $N = 40.89 \pm 9.79$ (at 215 mW/cm²) and $N = 53.29 \pm 13.12$ (at 456 mW/cm²). It is important to note that introducing a 2 nm thick spacer increases the number of excitons by $\sim 10\times$, despite only having a $\sim 20\%$ decrease in the measured Rabi splitting. From the g -field mapping, introducing a 2 nm spacer leads to a $\sim 72\%$ decrease in the coupling strength from ~ 25 meV to ~ 7 meV, which is attributed to weaker plasmonic fields 2 nm away from the gold surface. This is also reflected from the mode area of the plasmonic mode, which increases from $A_{\text{mod}} = 146$ nm² (for the TMD dimer case) to $A_{\text{mod}} = 1130$ nm² (for TMD spacer dimer case). This indicates that the plasmonic field in the TMD plane is less confined and constitutes a larger mode area, thereby incorporating more excitons in the coupling.

Apart from tuning the spatial field overlap between the dimer antenna and the monolayer WS₂, it is also possible to employ dielectric coating for tuning resonance mode positions. This is illustrated in the study of strong coupling between a synthesized silver nanorod on monolayer WSe₂ [46], where the resonance mode is red shifted by conformally coating the nanorod at increasing dielectric thicknesses. In our work, however, the dielectric spacer was used only for tuning the spatial field overlap. Another difference lies in the use of the fundamental plasmonic mode of the dimer antenna in this work, in contrast to the higher-order plasmonic mode in [46]. These modes exhibit different mode areas, which result in a huge difference in the number of excitons between our work and the work in [46]. As a further validation of our approach, we estimate the number of excitons from the literature and perform a direct comparison with their reported numbers (Table 1). More detailed calculations for these comparisons are given in Table S1 in Supplement 1. As shown in Table 1, the numbers of excitons deduced by our method are comparable to the reported numbers, despite the apparent differences of how the number of excitons is deduced in other works. We note that the

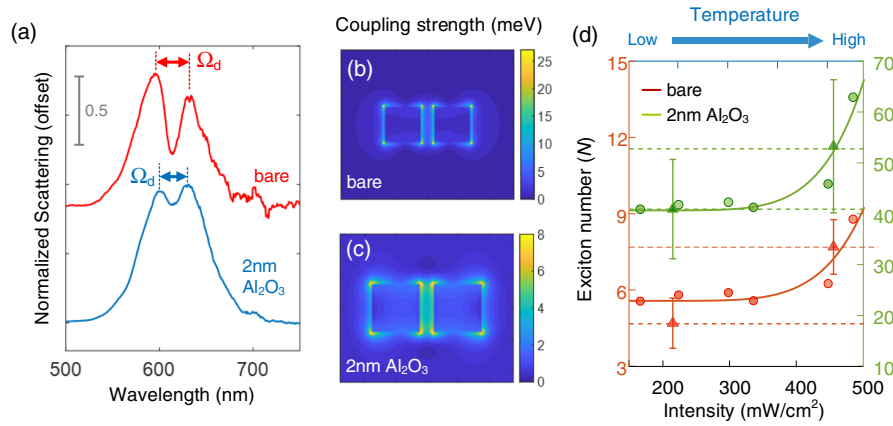


Fig. 4. Effect of plasmon-assisted heating in number of excitons. (a) Normalized scattering spectra of TMD dimer (red) and TMD spacer dimer (blue) systems, with the dimer structures chosen to represent the most symmetrical spectral splitting: size = 60 nm, gap = 20 nm (bare), and size = 80 nm, gap = 20 nm (with 2 nm Al_2O_3 spacer). (b)–(c) Mapping of coupling strength for (b) TMD dimer and (c) TMD spacer dimer systems at the TMD top surface. (d) Exciton number (N) for TMD dimer (red) and TMD spacer dimer (green) cases at different temperatures. The experimentally deduced exciton numbers are indicated by the flat dashed lines with triangle markers: (TMD dimer) $N = 4.67 \pm 0.99$ (at $215 \text{ mW}/\text{cm}^2$), $N = 7.69 \pm 1.07$ (at $456 \text{ mW}/\text{cm}^2$); (TMD spacer dimer) $N = 40.89 \pm 9.79$ (at $215 \text{ mW}/\text{cm}^2$), $N = 53.29 \pm 13.12$ (at $456 \text{ mW}/\text{cm}^2$). The numbers of excitons obtained from full-wave simulation with temperature-dependent gold permittivity are shown in circle markers fitted by solid curves.

Table 1. Reported Strong Coupling Characteristics and Exciton Numbers in Nanoparticle on Metal (NPOm) and Planar Antenna Structures

Structure	Platform	Ω (meV)	N	Estimated N (Our method)	Reference
Ag Nanorod on WSe_2 on SiO_2	Planar	49.5	~ 4100	6267	Zheng <i>et al.</i> [46]
Ag nanocube on WSe_2 on $\text{Al}_2\text{O}_3/\text{Au}$	NPOm	36.7	~ 816	~ 373	Sun <i>et al.</i> [40]
Ag nanocube on WS_2 on $\text{Al}_2\text{O}_3/\text{Ag}$	NPOm	145	~ 130	~ 90	Han <i>et al.</i> [34]
Au nanorod on WS_2 on SiO_2	Planar	113.8	~ 13.8	~ 11.5	Wen <i>et al.</i> [47]
TMD Dimer	Planar	115.2–128.6	–	$\sim 4.67 - 7.69$	This work
TMD Spacer Dimer	Planar	100.2–100.7	–	$\sim 40.89 - 53.29$	This work

large increase of excitons upon dielectric spacer insertion in our work corroborates with the large numbers of excitons in strongly coupled NPOm systems whose mechanisms mainly depend on the ultrathin spacer between the antenna and the mirror [30,34,40]. This is attributed to the dominant out-of-plane (E_z) E -field in NPOm resonance modes, which does not couple to the in-plane transition dipole moments of the TMD. According to our finite-difference time-domain simulations of these NPOm systems (Table S1 in Supplement 1), the in-plane E -fields $|E_{xy}|$ are typically $\sim 2 - 3 \times$ smaller compared to the total cavity mode field $|E_{\text{tot}}|$. Meanwhile, for planar antennas, introducing a dielectric spacer increases the out-of-plane components in the TMD, resulting in a decrease of coupling to the in-plane excitons. This is illustrated in the comparison of total and in-plane mode fields for TMD dimer and TMD spacer dimer systems in Fig. S1 in Supplement 1.

The intensity-dependent thermal effects are observed from the $\sim 64\%$ and $\sim 30\%$ increases in the number of excitons, as the incident intensity is increased from $215 \text{ mW}/\text{cm}^2$ to $456 \text{ mW}/\text{cm}^2$, for the TMD dimer and TMD spacer dimer, respectively. To further understand the relation between the thermal effects and the number of excitons, we simulate the split resonance characteristics in the TMD dimer system at different temperatures, using the temperature-dependent Au permittivity reported by Reddy *et al.* [48]. Here, the simulated number of excitons (N_{sim}) is obtained by the same approach as before, but with the measured coupling strength g_{exp} replaced by the simulated coupling strength g_{sim} ;

i.e., $N_{\text{sim}} = (g_{\text{sim}}/g_{\text{avg}})^2$. As shown in Fig. 4(d), the simulated N_{sim} (circle markers) is plotted as the temperature is increased, with the experimental N for different illumination intensities represented by triangle markers with error bars. By comparing the number of excitons in the TMD dimer (red) and the TMD spacer dimer (green) cases, a correlation between the increasing intensity and higher temperature can be seen. In addition, this also suggests the feasibility of using plasmon-induced heating as an active-tuning mechanism for strong-coupling characteristics, notably in the number of excitons.

We investigate the thermal effects further by characterizing photoluminescence of a single TMD spacer dimer system as a function of pumping intensities, as shown in Fig. 5. Photoluminescence of WS_2 (area curves) and TMD spacer dimer (solid curves) are plotted in Fig. 5(a) as the 532 nm pumping laser intensity is varied from $0.36 \text{ kW}/\text{cm}^2$ to $16.2 \text{ kW}/\text{cm}^2$. At increasing pumping intensity, the PL peak position of the coupled dimer undergoes a red shift, while that of the bare WS_2 is almost unaffected. Such a red shift is attributed to the increase of electron–electron and electron–phonon scattering inside the gold nanostructures, as the temperature increases, which translates to a higher damping loss and thus a larger imaginary part of the gold permittivity [48].

We note that the red shifting is not as large as in Hg lamp scattering measurements, despite the much higher pump intensity. The differences are attributed to different excitation frequencies in our scattering and PL experiments. The spectrum of the Hg

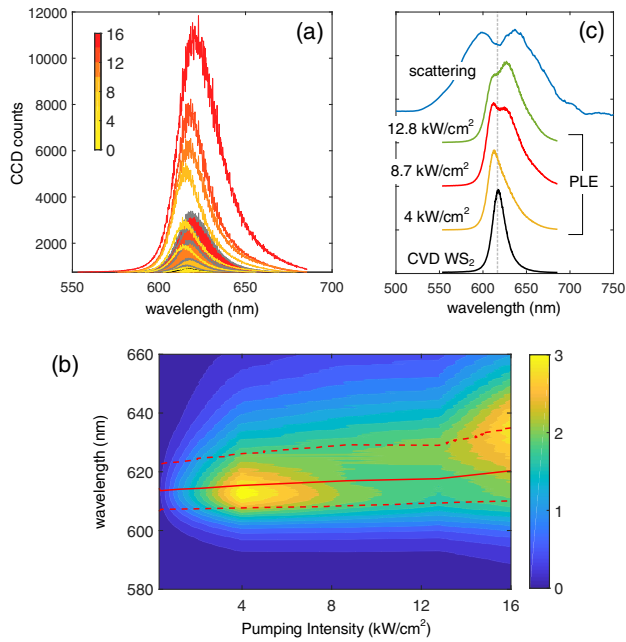


Fig. 5. Temperature-dependent photoluminescence characteristics of plasmon–exciton system. (a) PL spectra of WS_2 (area curves) and TMD spacer dimer (solid curves) as the pumping intensity is varied from 0.36 kW/cm^2 to 16.2 kW/cm^2 . (b) PL intensity enhancement (PLE) as a function of pumping intensity, with the peak positions and emission linewidth indicated by the red solid line and red dashed lines, respectively. (c) Red shifting of the PLE spectra at 4 kW/cm^2 , 8.7 kW/cm^2 and 12.8 kW/cm^2 , compared to the normalized scattering spectra of the TMD spacer dimer system (size = 100 nm , gap = 40 nm).

lamp used in scattering experiment, is known to comprise multiple excitation peaks at 337 nm , 365 nm , 405 nm , 436 nm , 546 nm , 577 nm , and 579 nm . This is in contrast to the continuous wave 532 nm laser used in our PL experiments. The many excitation peaks and the flat background spectrum of the Hg lamp, despite their lower combined intensity, would have different plasmonic heating effects than a single excitation peak of the 532 nm laser in the PL experiment. We also note that both scattering and PL experiments also differed in the collection time (see Appendix A.2, Optical Characterization), indicating that the collection time in the PL system is far shorter than in the scattering experiment. Another likely factor is the fact that PL relies mainly on the absorption rather than on the scattering paths. In addition, the pumping wavelength (532 nm) is off-resonant to the plasmonic nanoantenna that has a resonance near the WS_2 emission wavelength (620 nm). The significant differences in the red shifting between the coupled and uncoupled systems demonstrate the role of the plasmon-induced heating in the PL response. To see the PL response from the nanoantenna, we subtract the PL response from that of the bare WS_2 , and define the PL intensity enhancement by $\text{PLE} = (\text{PL}_{\text{dimer}} - \text{PL}_{\text{WS}_2}) / \text{PL}_{\text{WS}_2}$. The mapping of the PLE as a function of pumping intensity is shown in Fig. 5(b), alongside with their PL peak positions (solid red) and full-width at half-maximum (dashed red).

The observed ~ 3 -fold direct PL intensity enhancement is in good agreement with other studies of WS_2 coupled with a circular dimer [49]. The PLE peaks appear to be within the linewidth of the PL response of the coupled nanoantenna, which, at increasing pumping intensity, appears to move from one side of the spectra (at $\sim 4 \text{ kW/cm}^2$) toward the other (at $\sim 16 \text{ kW/cm}^2$). As the PL

intensity enhancement is facilitated by a strong plasmonic field and radiation modification, we interpret the shorter wavelength PLE peak (at 4 kW/cm^2) to be the result of plasmonic resonance at the shorter wavelength. Due to plasmon-induced heating at the increasing pumping intensity (to about $8 - 12 \text{ kW/cm}^2$), the plasmonic resonance is tuned across the WS_2 emission, manifesting in spectral splitting when the plasmonic resonance is closely detuned from the WS_2 exciton, resembling the split resonances in the dark-field scattering. Figure 5(c) illustrates the red shifting of the PLE spectra at 4 kW/cm^2 , 8.7 kW/cm^2 and 12.8 kW/cm^2 , compared to the PL response of the bare WS_2 and the scattering of the same dimer ($s = 100 \text{ nm}$, $d = 40 \text{ nm}$). The spectral splitting in the PLE is found to be narrower than that of the dark-field scattering. We attribute this to the absorption and radiation pathways associated with the photoluminescence and scattering processes. This is supported by our numerical simulations, which show that the splitting in the absorption cross-sections is narrower than that in the scattering cross-sections. Other works by Wersäll *et al.* seems to verify this in their investigation of PL splitting in J-aggregates coupled to Ag nanoprisms at a 4 K temperature [31].

3. CONCLUSION

In summary, we have presented a detailed study of a strongly coupled plasmon–exciton system at a few-excitons level and investigated the feasibility of plasmon-induced heating as an active tuning mechanism of strong coupling. Given the concentration of the local E -fields at plasmonic hot spots, coupled with the plasmon–exciton interaction occurring only in the TMD plane, we deduce the number of excitons from spatially averaging the positionally dependent coupling strength in the TMD plane. We demonstrate that our strongly coupled system consists of $N = 4.67 \pm 0.99$ excitons, which change dramatically to $N = 40.89 \pm 9.79$ as a 2 nm thick dielectric spacer is inserted between the monolayer TMD and plasmonic nanoantenna. Such ~ 10 -fold increase in the number of excitons corresponds to a $\sim 72\%$ decrease in the coupling strength per exciton, thereby illustrating the confounding effects of the coupling strength and number of excitons in the observed Rabi splitting in strongly coupled systems. Furthermore, the number of excitons is also found to be dependent on plasmon-induced heating effects, which was demonstrated experimentally in the statistically significant change in the number of excitons from $N = 4.67 \pm 0.99$ to $N = 7.69 \pm 1.07$, as the illumination intensity is increased from 215 mW/cm^2 to 456 mW/cm^2 . Equally interesting is the observation that the change of Rabi splitting is more statistically significant in the plasmon–exciton system without a dielectric spacer. This verifies the dependence of intensity-dependent thermal effects on the spatial mode overlap between the plasmonic field and the TMD. Further investigation of the plasmon-induced thermal effects is in the red shifting of photoluminescence enhancements for a single dimer at different pumping intensities. The signature of the strong coupling is observed at $8 - 12 \text{ kW/cm}^2$ pumping intensity range, where the plasmonic resonance is close to the exciton emission. Finally, the observed narrower spectral splitting in the PL enhancements, as compared to that of the scattering, is attributed to the absorption and radiation pathways associated with the photoluminescence and scattering processes, respectively.

APPENDIX A: METHODS

1. Sample Fabrication

The monolayer WS₂ was CVD-grown on 295 nm thick thermal oxide on silicon substrate (from 2Dsemiconductors USA). The plasmonic nanoantennas were fabricated via electron beam lithography (EBL) and lift-off pattern transfer. The EBL patterning was carried out by series of line exposures with 20 kV energy and 30 pA beam current on 120 nm thick ZEP520A *e*-beam resist, followed by sonicated cold development in a mixture of *n*-pentyl acetate and isopropanol alcohol at 6°C temperature. 30 nm thick gold was then physically deposited on the sample, and subject to lift-off pattern transfer in *n*-methyl pyrrolidone (NMP) at 60°C for 10 mins. For dielectric spacer layer insertion, atomic layer deposition (Ultratech/Cambridge NanoTech) was used to conformally coat a 2 nm thick Al₂O₃ layer on WS₂/SiO₂/Si sample before nanoantenna patterning.

2. Optical Characterization

The plasmonic nanoantennas and the plasmon–exciton systems were characterized by hyperspectral imaging system (Fig. S2, Supplement 1), using either a broadband halogen or mercury (Hg) lamp as the light source. All measurements were conducted in dark-field geometry with a 50× objective lens (NA = 0.55), where the sample was scanned via piezo-controlled stage at a scanning speed (Δt) of 0.5–1s per line. The total scanning time is $t_{\text{tot}} = N_{\text{line}} \times \Delta t$, with N_{line} as the number of lines in the image. Typical scanning time is 10–15 min. The low-powered halogen lamp was used to measure the scattering characteristics of uncoupled plasmonic nanoantennas, while the Hg lamp was used to measure strong coupling characteristics of the plasmon–exciton systems. To eliminate the polarization mixing, we used polarizers after the source and before the spectrometer. Given all the nanoantennas investigated in this work are planar dimers, all the scattering measurements were conducted under *x*-polarization (i.e., along the long axis of the dimer). For photoluminescence measurements, we used WITec system (Alpha300) with 532 nm laser and 100× objective lens (NA = 0.8). The incident power of the 532 nm laser was characterized by an optical power meter, with a laser spot of $\sim 1 \mu\text{m}$ based on 100× objective lens. The integration time was set to 0.5s, and the PL was averaged 3 times. For the Hg lamp, the beam spots were characterized from image of reference grids at different lens magnifications at low power (to prevent image saturation), giving beam spots of $\sim 2.48 \text{ mm}$ (for a 10× objective lens) and $\sim 0.86 \text{ mm}$ (for a 50× objective lens). The incident intensities were then obtained by dividing the measured power (by the same optical power meter) with the beam spot area.

3. Numerical Calculations

The commercial finite-difference time-domain software (FDTD Solutions, Lumerical Inc.) was used for the full-wave simulation. The monolayer WS₂ is modeled as a 0.618 nm thick dielectric layer, whose permittivity was modeled as a Lorentzian oscillator $\epsilon(E) = 1 + \sum_{k=1}^N f_k / (E_k^2 - E^2 - i\gamma_k E)$, where f_k and γ_k are the oscillator strength and the linewidth of the k th oscillator, and E_k is the oscillation energy that runs over the full spectral range [50,51]. The permittivity of the gold for different temperatures was obtained from Reddy *et al.* [48], while those of silicon and Al₂O₃ were taken from the software database.

Funding. Ministry of Education—Singapore (MOE2018-T2-1-176, MOE2018-T2-2-189(S)); Agency for Science, Technology and Research (1720700038, A1883c0002, A18A7b0058, A20E5c0095); National Research Foundation Singapore (NRF-CRP22-2019-0006, NRF-CRP23-2019-0007); Agencia Estatal de Investigación (CEX2018-000805-M, PCI2018-093145, RTI2018-099737-B-I00).

Acknowledgment. The authors acknowledge Antonio Isaac Fernández-Domínguez for valuable discussions about the calculations of the exciton number and the Nanyang Nanofabrication Centre (N2FC) for facilitating the device fabrication.

Disclosures. The authors declare no conflict of interest.

Data availability. Data underlying the results presented in this paper are not publicly available at this time but may be obtained from the authors upon reasonable request.

Supplemental document. See Supplement 1 for supporting content.

[†]These authors contributed equally to this work.

REFERENCES

1. Y. Yamamoto, H. Deng, and H. Haug, “Bose-Einstein condensation of exciton-polaritons,” *Riv. Nuovo Cim.* **33**, 591–631 (2010).
2. H. Deng, H. Haug, and Y. Yamamoto, “Exciton-polariton Bose-Einstein condensation,” *Rev. Mod. Phys.* **82**, 1489–1537 (2010).
3. H. Deng, G. Weihs, C. Santori, J. Bloch, and Y. Yamamoto, “Condensation of semiconductor microcavity exciton polaritons,” *Science* **298**, 199–202 (2002).
4. T. Byrnes, N. Y. Kim, and Y. Yamamoto, “Exciton-polariton condensates,” *Nat. Phys.* **10**, 803–813 (2014).
5. L. Dominici, G. Dagvadorj, J. M. Fellows, D. Ballarini, M. De Giorgi, F. M. Marchetti, B. Piccirillo, L. Marrucci, A. Bramati, G. Gigli, M. H. Szymańska, and D. Sanvitto, “Vortex and half-vortex dynamics in a nonlinear spinor quantum fluid,” *Sci. Adv.* **1**, e1500807 (2015).
6. L. Chang, X. Jiang, S. Hua, C. Yang, J. Wen, L. Jiang, G. Li, G. Wang, and M. Xiao, “Parity-time symmetry and variable optical isolation in active-passive-coupled microresonators,” *Nat. Photonics* **8**, 524–529 (2014).
7. R. El-Ganainy, K. G. Makris, M. Khajavikhan, Z. H. Musslimani, S. Rotter, and D. N. Christodoulides, “Non-Hermitian physics and PT symmetry,” *Nat. Phys.* **14**, 11–19 (2018).
8. D. Ballarini, M. De Giorgi, E. Cancellieri, R. Houdre, E. Giacobino, R. Cingolani, A. Bramati, G. Gigli, and D. Sanvitto, “All-optical polariton transistor,” in *Conf. Lasers Electro-Optics Eur. Int. Quantum Electron. Conf. (CLEO/Europe-IQEC)* (2013).
9. A. V. Zasedatelev, A. V. Baranikov, D. Urbonas, F. Scafirimuto, U. Scherf, T. Stöferle, R. F. Mahrt, and P. G. Lagoudakis, “A room-temperature organic polariton transistor,” *Nat. Photonics* **13**, 378–383 (2019).
10. T. Gao, P. S. Eldridge, T. C. H. Liew, S. I. Tsintzos, G. Stavrinidis, G. Deligeorgis, Z. Hatzopoulos, and P. G. Savvidis, “Polariton condensate transistor switch,” *Phys. Rev. B* **85**, 235102 (2012).
11. T. G. Tiecke, J. D. Thompson, N. P. De Leon, L. R. Liu, V. Vuletić, and M. D. Lukin, “Nanophotonic quantum phase switch with a single atom,” *Nature* **508**, 241–244 (2014).
12. J. McKeever, A. Boca, A. D. Boozer, J. R. Buck, and H. J. Kimble, “Experimental realization of a one-atom laser in the regime of strong coupling,” *Nature* **425**, 268–271 (2003).
13. I. Pockrand, J. D. Swalen, R. Santo, A. Brillante, and M. R. Philpott, “Optical properties of organic dye monolayers by surface plasmon spectroscopy,” *J. Chem. Phys.* **69**, 4001–4011 (1978).
14. A. I. Väkeväinen, R. J. Moerland, H. T. Rekola, A.-P. Eskelinen, J.-P. Martikainen, D.-H. Kim, and P. Törmä, “Plasmonic surface lattice resonances at the strong coupling regime,” *Nano Lett.* **14**, 1721–1727 (2014).
15. T. K. Hakala, J. J. Toppari, A. Kuzyk, M. Pettersson, H. Tikkanen, H. Kunttu, and P. To, “Vacuum Rabi splitting and strong-coupling dynamics for surface-plasmon polaritons and rhodamine 6G molecules,” *Phys. Rev. Lett.* **103**, 053602 (2009).
16. D. E. Gómez, K. C. Vernon, P. Mulvaney, and T. J. Davis, “Surface plasmon mediated strong exciton–photon coupling in semiconductor nanocrystals,” *Nano Lett.* **10**, 274–278 (2010).

17. D. E. Gómez, K. C. Vernon, P. Mulvaney, and T. J. Davis, "Coherent superposition of exciton states in quantum dots induced by surface plasmons," *Appl. Phys. Lett.* **96**, 073108 (2010).
18. J. Dintinger, S. Klein, F. Bustos, W. L. Barnes, and T. W. Ebbesen, "Strong coupling between surface plasmon-polaritons and organic molecules in subwavelength hole arrays," *Phys. Rev. B* **71**, 035424 (2005).
19. J. Dintinger, S. Klein, and T. W. Ebbesen, "Molecule-surface plasmon interactions in hole arrays: enhanced absorption, refractive index changes, and all-optical switching," *Adv. Mater.* **18**, 1267–1270 (2006).
20. Y. Sugawara, T. A. Kelf, J. J. Baumberg, M. E. Abdelsalam, and P. N. Bartlett, "Strong coupling between localized plasmons and organic excitons in metal nanovoids," *Phys. Rev. Lett.* **97**, 266808 (2006).
21. G. A. Wurtz, P. R. Evans, W. Hendren, R. Atkinson, W. Dickson, R. J. Pollard, A. V. Zayats, W. Harrison, and C. Bower, "Molecular plasmonics with tunable exciton-plasmon coupling strength in J-aggregate hybridized Au nanorod assemblies," *Nano Lett.* **7**, 1297–1303 (2007).
22. J. Bellessa, C. Symonds, K. Vynck, A. Lemaitre, A. Brioude, L. Beaur, J. C. Plenet, P. Viste, D. Felbacq, E. Cambril, and P. Valvin, "Giant Rabi splitting between localized mixed plasmon-exciton states in a two-dimensional array of nanosize metallic disks in an organic semiconductor," *Phys. Rev. B* **80**, 033303 (2009).
23. K. F. Mak and J. Shan, "Photonics and optoelectronics of 2D semiconductor transition metal dichalcogenides," *Nat. Photonics* **10**, 216–226 (2016).
24. X. Duan, C. Wang, A. Pan, R. Yu, and X. Duan, "Two-dimensional transition metal dichalcogenides as atomically thin semiconductors: opportunities and challenges," *Chem. Soc. Rev.* **44**, 8859–8876 (2015).
25. X. Liu, T. Galfsky, Z. Sun, F. Xia, E. C. Lin, Y. H. Lee, S. Kéna-Cohen, and V. M. Menon, "Strong light-matter coupling in two-dimensional atomic crystals," *Nat. Photonics* **9**, 30–34 (2014).
26. R. F. Ribeiro, L. A. Martínez-Martínez, M. Du, J. Campos-Gonzalez-Angulo, and J. Yuen-Zhou, "Polariton chemistry: controlling molecular dynamics with optical cavities," *Chem. Sci.* **9**, 6325–6339 (2018).
27. V. A. Shahnazaryan, V. A. Saroka, I. A. Shelykh, W. L. Barnes, and M. E. Portnoi, "Strong light-matter coupling in carbon nanotubes as a route to exciton brightening," *ACS Photon.* **6**, 904–914 (2019).
28. E. Cohen-Hoshen, G. W. Bryant, I. Pinkas, J. Sperling, and I. Bar-Joseph, "Exciton-plasmon interactions in quantum dot-gold nanoparticle structures," *Nano Lett.* **12**, 4260–4264 (2012).
29. A. E. Schlather, N. Large, A. S. Urban, P. Nordlander, and N. J. Halas, "Near-field mediated plexcitonic coupling and giant Rabi splitting in individual metallic dimers," *Nano Lett.* **13**, 3281–3286 (2013).
30. G. Zengin, M. Wersäll, S. Nilsson, T. J. Antosiewicz, M. Käll, and T. Shegai, "Realizing strong light-matter interactions between single-nanoparticle plasmons and molecular excitons at ambient conditions," *Phys. Rev. Lett.* **114**, 157401 (2015).
31. M. Wersäll, J. Cuadra, T. J. Antosiewicz, S. Balci, and T. Shegai, "Observation of mode splitting in photoluminescence of individual plasmonic nanoparticles strongly coupled to molecular excitons," *Nano Lett.* **17**, 551–558 (2017).
32. S. Balci, "Ultrastrong plasmon-exciton coupling in metal nanoprisms with J-aggregates," *Opt. Lett.* **38**, 4498–4501 (2013).
33. S. Hou, L. Y. M. Tobing, X. Wang, Z. Xie, J. Yu, J. Zhou, D. Zhang, C. Dang, P. Coquet, B. K. Tay, M. D. Birowosuto, E. H. T. Teo, and H. Wang, "Manipulating coherent light-matter interaction: continuous transition between strong coupling and weak coupling in MoS₂ monolayer coupled with plasmonic nanocavities," *Adv. Opt. Mater.* **7**, 1900857 (2019).
34. X. Han, K. Wang, X. Xing, M. Wang, and P. Lu, "Rabi splitting in a plasmonic nanocavity coupled to a WS₂ monolayer at room temperature," *ACS Photon.* **5**, 3970–3976 (2018).
35. J. Cuadra, D. G. Baranov, M. Wersäll, R. Verre, T. J. Antosiewicz, and T. Shegai, "Observation of tunable charged exciton polaritons in hybrid monolayer WS₂-plasmonic nanoantenna system," *Nano Lett.* **18**, 1777–1785 (2018).
36. M.-E. Kleemann, R. Chikkaraddy, E. M. Alexeev, D. Kos, C. Carnegie, W. Deacon, A. C. de Pury, C. Große, B. de Nijs, J. Mertens, A. I. Tartakovskii, and J. J. Baumberg, "Strong-coupling of WSe₂ in ultra-compact plasmonic nanocavities at room temperature," *Nat. Commun.* **8**, 1296 (2017).
37. R. Liu, Z.-K. K. Zhou, Y.-C. C. Yu, T. Zhang, H. Wang, G. Liu, Y. Wei, H. Chen, and X.-H. H. Wang, "Strong light-matter interactions in single open plasmonic nanocavities at the quantum optics limit," *Phys. Rev. Lett.* **118**, 237401 (2017).
38. K. Santhosh, O. Bitton, L. Chuntonov, and G. Haran, "Vacuum Rabi splitting in a plasmonic cavity at the single quantum emitter limit," *Nat. Commun.* **7**, 11823 (2016).
39. R. Chikkaraddy, B. de Nijs, F. Benz, S. J. Barrow, O. A. Scherman, E. Rosta, A. Demetriadou, P. Fox, O. Hess, and J. J. Baumberg, "Single-molecule strong coupling at room temperature in plasmonic nanocavities," *Nature* **535**, 127–130 (2016).
40. J. Sun, H. Hu, D. Zheng, D. Zhang, Q. Deng, S. Zhang, and H. Xu, "Light-emitting plexciton: exploiting plasmon-exciton interaction in the intermediate coupling regime," *ACS Nano* **12**, 10393–10402 (2018).
41. B. W. Shore and P. L. Knight, "The Jaynes-Cummings model," *J. Mod. Opt.* **40**, 1195–1238 (1993).
42. S. Pau, G. Björk, J. Jacobson, H. Cao, and Y. Yamamoto, "Microcavity exciton-polariton splitting in the linear regime," *Phys. Rev. B* **51**, 14437–14447 (1995).
43. G. Khitrova, A. Scherer, C. Ell, H. M. Gibbs, J. Hendrickson, T. Yoshie, O. B. Shchekin, D. G. Deppe, and G. Rupper, "Vacuum Rabi splitting with a single quantum dot in a photonic crystal nanocavity," *Nature* **432**, 200–203 (2004).
44. J. Feldmann, G. Peter, E. O. Göbel, P. Dawson, K. Moore, C. Foxon, and R. J. Elliott, "Linewidth dependence of radiative exciton lifetimes in quantum wells," *Phys. Rev. Lett.* **59**, 2337 (1987).
45. E. J. Sie, J. W. McIver, Y.-H. Lee, L. Fu, J. Kong, and N. Gedik, "Optical Stark effect in 2D semiconductors," *Proc. SPIE* **9835**, 983518 (2016).
46. D. Zheng, S. Zhang, Q. Deng, M. Kang, P. Nordlander, and H. Xu, "Manipulating coherent plasmon-exciton interaction in a single silver nanorod on monolayer WSe₂," *Nano Lett.* **17**, 3809–3814 (2017).
47. J. Wen, H. Wang, W. Wang, Z. Deng, C. Zhuang, Y. Zhang, F. Liu, J. She, J. Chen, H. Chen, S. Deng, and N. Xu, "Room-temperature strong light-matter interaction with active control in single plasmonic nanorod coupled with two-dimensional atomic crystals," *Nano Lett.* **17**, 4689–4697 (2017).
48. H. Reddy, U. Guler, A. V. Kildishev, A. Boltasseva, and V. M. Shalaev, "Temperature-dependent optical properties of gold thin films," *Opt. Mater. Express* **6**, 2776–2802 (2016).
49. M. H. Tahersima, M. D. Birowosuto, Z. Ma, W. C. Coley, M. D. Valentin, S. Naghibi Alivillar, I.-H. Lu, Y. Zhou, I. Sarpkaya, A. Martinez, I. Liao, B. N. Davis, J. Martinez, D. Martinez-Ta, A. Guan, A. E. Nguyen, K. Liu, C. Soci, E. Reed, L. Bartels, and V. J. Sorger, "Testbeds for transition metal dichalcogenide photonics: efficacy of light emission enhancement in monomer vs dimer nanoscale antennae," *ACS Photon.* **4**, 1713–1721 (2017).
50. Y. Li, A. Chernikov, X. Zhang, A. Rigosi, H. M. Hill, A. M. Van Der Zande, D. A. Chenet, E. M. Shih, J. Hone, and T. F. Heinz, "Measurement of the optical dielectric function of monolayer transition-metal dichalcogenides: MoS₂, MoSe₂, WS₂, and WSe₂," *Phys. Rev. B* **90**, 205422 (2014).
51. A. Laturia, M. L. Van de Put, and W. G. Vandenberghe, "Dielectric properties of hexagonal boron nitride and transition metal dichalcogenides: from monolayer to bulk," *npj 2D Mater. Appl.* **2**, 1–7 (2018).